A&A 414, 857–872 (2004)
DOI: 10.1051/0004-6361:20031664

Astronomy & Astrophysics

Molecular gas in NUclei of GAlaxies (NUGA)

II. The ringed LINER NGC 7217⋆

F. Combes[1], S. García-Burillo[2], F. Boone[3], L. K. Hunt[4], A. J. Baker[5], A. Eckart[6], P. Englmaier[7], S. Leon[8], R. Neri[9], E. Schinnerer[10], and L. J. Tacconi[5]

[1] Observatoire de Paris, LERMA, 61 Av. de l'Observatoire, 75014 Paris, France
[2] Observatorio Astronómico Nacional (OAN), Alfonso XII, 3, 28014 Madrid, Spain
[3] Bochum University, Universitätstrasse 150, 44780 Bochum, Germany
[4] Istituto di Radioastronomia/CNR, Largo Enrico Fermi 5, 50125 Firenze, Italy
[5] Max-Planck-Institut für extraterrestrische Physik, Postfach 1312, 85741 Garching, Germany
[6] I. Physikalisches Institut, Universität zu Köln, Zülpicherstrasse 77, 50937 Köln, Germany
[7] Astronomy, Universität Basel, Venusstrasse 7, CH 4102 Binningen, Switzerland
[8] Instituto de Astrofísica de Andalucía (CSIC), Camino Bajo de Huétor, 24, 18008 Granada, Spain
[9] IRAM-Institut de Radio Astronomie Millimétrique, 300 Rue de la Piscine, 38406 St. Mt. d'Hères, France
[10] NRAO, PO Box 0, Socorro, NM-87801, USA

Received 14 May 2003 / Accepted 24 October 2003

Abstract. We present CO(1–0) and CO(2–1) maps of the LINER galaxy NGC 7217, obtained with the IRAM interferometer, at $2.4'' \times 1.9''$ and $1.2'' \times 0.8''$ resolution respectively. The nuclear ring (at $r = 12'' = 0.8$ kpc) dominates the CO maps, and has a remarkable sharp surface density gradient at its inner edge. The latter is the site of the stellar/Hα ring, while the CO emission ring extends farther or is broader (500−600 pc). This means that the star formation has been more intense toward the inner edge of the CO ring, in a thin layer, just at the location of the high gas density gradient. The CO(2–1)/CO(1–0) ratio is close to 1, typical of warm optically thick gas with high density. The overall morphology of the ring is quite circular, with no evidence of non-circular velocities. In the CO(2–1) map, a central concentration might be associated with the circumnuclear ionized gas detected inside $r = 3''$ and interpreted as a polar ring in the literature. The CO(2–1) emission inside $3''$ coincides with a spiral dust lane, clearly seen in the HST $V - I$ color image.
N-body simulations including gas dissipation and star formation are performed to better understand the nature of the nuclear ring observed. The observed rotation curve of NGC 7217 allows two possibilities, according to the adopted mass for the disk: (1) either the disk is massive, allowing a strong bar to develop, or (2) it is dominated in mass by an extended bulge/stellar halo, and supports only a mild oval distortion. The amount of gas also plays an important role in the disk stability, and therefore the initial gas fraction was varied, with star formation reducing the total gas fraction to the observed value. The present observations support *only* the bulge-dominated model, which is able to account for the nuclear ring in CO and its position relative to the stellar and Hα ring. In this model, the gas content was higher in the recent past (having been consumed via star formation), and the structures formed were more self-gravitating. Only a mild bar formed, which has now vanished, but the stars formed in the highest gas density peaks toward the inner edge of the nuclear ring, which corresponds to the observed thin stellar ring. We see no evidence for an ongoing fueling of the nucleus; instead, gas inside the ring is presently experiencing an outward flow. To account for the nuclear activity, some gas infall and fueling must have occured in the recent past (a few Myr ago), since some, albeit very small, CO emission is detected at the very center. These observations have been made in the context of the NUclei of GAlaxies (NUGA) project, aimed at the study of the different mechanisms for gas fueling of AGN.

Key words. galaxies: general – galaxies: ISM – galaxies: active – galaxies: nuclei – galaxies: individual: NGC 7217

1. Introduction

Accretion onto black holes has become the accepted explanation for nuclear activity in galaxies. But while most galaxies are now thought to harbor central massive black holes, only a fraction of them host active nuclei (AGNs). The reasons for this have been the subject of much investigation, but it remains unclear whether the explanation lies in the total gas mass available for fueling the AGN or in the mechanism by which fuel is funneled into the central pc.

The main problem for fueling the AGN is the removal of angular momentum from the disk gas, a process which can be accomplished through non-axisymmetric perturbations.

Send offprint requests to: F. Combes,
e-mail: francoise.combes@obspm.fr

⋆ Based on observations carried out with the IRAM Plateau de Bure Interferometer and IRAM 30 m telescope. IRAM is supported by INSU/CNRS (France), MPG (Germany) and IGN (Spain).

These might be of external origin, triggered by a companion (Heckman et al. 1986), or internal due to density waves such as bars or spirals, and their gravity torques (e.g. Combes 2001). The distinction is sometimes difficult to make, since the tidal interaction of companions triggers bar formation in the target disk.

Nevertheless, the presence of a bar is not necessarily associated with AGNs (Mulchaey & Regan 1997; Knapen et al. 2000), and the fueling processes might involve more localised phenomena, such as embedded nuclear bars (Shlosman et al. 1989), lopsidedness or $m = 1$ instabilities (Shu et al. 1990; Kormendy & Bender 1999; García-Burillo et al. 2000) or the presence of warped nuclear disks (Pringle 1996; Schinnerer et al. 2000, 2000). To account for the non-correlation between bars and nuclear activity, there must be time delays between the first gas inflow due to the bar or spiral density waves, which first drive a nuclear starburst, and the subsequent fueling of the black hole, for example by the tidal disruption of stars in the just-formed nuclear stellar clusters. Once the gas has reached sufficiently small radii, the dynamical friction exerted by bulge stars on the giant molecular clouds can also provide a fueling mechanism (e.g. Stark et al. 1991).

The study of molecular gas morphology and dynamics constitutes an ideal tool for investigating AGN fueling, and its connection with circumnuclear star formation. Molecular gas is the dominant phase of the interstellar medium in the central kiloparsec of spiral galaxies, whereas the atomic gas is deficient there. This makes CO lines ideal to trace the dynamics of the interstellar medium and radial gas flows. However, to compare all the possible mechanisms to observations, high-resolution (1−2 arcsec) maps of the molecular component in the centers of galaxies are required. Previous surveys of molecular gas in active galaxies have been carried out by other groups (Heckman et al. 1989; Meixner et al. 1990; Vila-Vilaro et al. 1998), but have had insufficient spatial resolution to resolve the nuclear disk structures, or were limited to small samples (Tacconi et al. 1997; Baker 2000). This paper is the second of a series which describes on a case-by-case basis the results of the NUGA (or NUclei of GAlaxies) project. A detailed description of NUGA is given in García-Burillo et al. (2003) and Paper I (García-Burillo et al. 2003), which focuses on the counter-rotating system NGC 4826.

NGC 7217 ($D = 14.5$ Mpc: Buta et al. 1995, hereafter B95) is one of the first galaxies of the sample to have been mapped, and this paper describes the distribution and dynamics of its molecular gas. NGC 7217 is an isolated LINER 2 galaxy (Ho et al. 1997) of Hubble type (R)SA(r)ab. Its main characteristic is its high degree of axisymmetry, and the presence of three stellar rings, with radii of 0.75, 2.2 and 5.4 kpc. All three rings are young and bluer than the surrounding stellar disk (B95). The three rings are reminiscent of resonant rings in a barred galaxy (e.g. Buta & Combes 1996), although the galaxy is not barred, containing at most a weak oval perturbation (B95). The rings however could be the remnants of a previous bar episode in this galaxy, and it is interesting to note that one of the best correlations with nuclear activity level is the presence of outer rings (Hunt & Malkan 1999). Through numerical simulations of the gas response in the potential derived from a red image of NGC 7217, Buta et al. (1995) showed that even the present weak oval distortion was able to form the three observed resonant rings.

NGC 7217 is an early-type galaxy, and its bulge is particularly massive and extended. Merrifield & Kuijken (1994) claimed that a significant fraction (30%) of its stars are counter-rotating relative to the rest of the galaxy; however, Buta et al. (1995) interpreted this instead as a large velocity dispersion in the bulge. The bulge component is not only predominant in the center, but dominates the disk out to a large galactocentric distance. The disk of NGC 7217 is rather regular, and does not seem to possess a strong density wave; there is only flocculent multi-arm spiral structure, of varying prominence over the disk (cf. Table 2 for the various ring radii).

Hα imaging reveals a very neat and complete nuclear ring of ∼21″ diameter (Pogge 1989; Verdes-Montenegro et al. 1995), strikingly coincident with the blue stellar nuclear ring, but not with the nuclear dust ring; the latter is slightly interior, probably an effect of extinction (B95). In this paper, we compare the CO maps obtained with the IRAM interferometer to HST/WFPC2, HST/NICMOS, and ground-based Hα maps, show that the diameters of the corresponding rings are different, and interpret them in the light of numerical modeling.

We perform N-body numerical simulations, including gas dissipation and star formation, in order to illustrate the proposed mechanisms, namely how star formation and/or dynamical effects can drive the evolution of the radius of the nuclear gas ring. The previous numerical simulations of gas flow in a fixed potential derived from a red image of the galaxy (B95) only tested the present disk perturbation and its pattern speed, but did not address its formation and evolution. Also, the new observations presented in this paper allow us to better constrain the models.

The CO observations, together with images at other wavelengths, are presented in Sect. 2, and the CO results in Sect. 3. Comparison with other wavelengths is performed in Sect. 4. Section 5 describes the star formation history and stellar populations as gleaned from the observations at other wavelengths, and how these relate to the molecular gas morphology. In Sect. 6 we briefly describe the code and numerical methods, followed by the results of our simulations in Sect. 7. Possible interpretations are discussed in Sects. 8 and 9 gives our conclusions.

2. Observations

2.1. IRAM single dish CO observations

To add the short spacings, we performed IRAM 30 m observations in a 3×3 raster pattern with 7″ spacing (see Fig. 2), in July 2002. We used 4 SIS receivers to observe simultaneously at the frequencies of the CO(1–0) and the CO(2–1) lines. At 115 GHz and 230 GHz, the telescope half-power beam widths are 22″ and 12″, respectively. The main-beam efficiency is $\eta_{\rm mb} = T_{\rm A}^*/T_{\rm mb} = 0.79$ at 115 GHz and 0.57 at 230 GHz. The typical system temperature varied between 200 and 450 K (on the $T_{\rm A}^*$ scale) at both frequencies. Wobbler switching mode was used, with reference positions offset by 4′

in azimuth. The pointing was regularly checked on continuum sources and the accuracy was 3″ rms. The backends were two 1 MHz filter banks and auto-correlator spectrometers. The total bandwidth available was 512 MHz at 115 GHz and 230 GHz, corresponding to 1300 km s^{-1} and 650 km s^{-1} for the CO(1–0) and CO(2–1) lines respectively (with velocity resolutions of 2.6 and 1.3 km s^{-1}).

Short spacings were then included using the SHORT-SPACE task in the GILDAS software (e.g. Guilloteau & Lucas 2000). Short spacings visibilities are computed from a map built by interpolation of the 30 m observations, deconvolved from the 30 m beam and multiplied by the PdB primary beam. The weights are adjusted in order to get the same mean weights in the single-dish data as in the interferometer data in the uv range of 1.25 D/λ to 2.5 D/λ (D = 15 m). All figures are made with short-spacing corrected data.

It is important to estimate the flux filtered out by the interferometric observations. With a beam of 45″ Young et al. (1995) measured a CO(1–0) flux toward the center of I(CO) = 2.27 K km s^{-1} (in the $T_{\rm A}^*$ scale). With a conversion factor of 42 Jy/K, their integrated flux is then S(CO) = 95 Jy km s^{-1}. Braine et al. (1993) with the IRAM-30 m measured I(CO) = 10 K km s^{-1} on average over a region of 36″diameter, yielding a flux of ∼120 Jy km s^{-1}. In the same region, we measure an average of 11 K km s^{-1} (and ∼130 Jy km s^{-1}), which is compatible. Here with the PdBI we measure 63 Jy km s^{-1} in the FOV = 43″ CO(1–0) map. We conclude that we have recovered about half of the flux in CO(1–0). In CO(2–1), with the single dish we measure 8 K km s^{-1}, compatible with Braine et al. (1993) who measured 9 K km s^{-1}, i.e. about 240 Jy km s^{-1} in integrated flux, in the inner 26″, and the interferometer measures only 24 Jy km s^{-1}. In this case, about 90% of the flux is missing, since the emission is not only extended, but also near the edge of our 21″ FOV (the mean radius of the CO ring being 12.5″).

2.2. IRAM interferometer CO observations

We observed the emission of the J = 1–0 and J = 2–1 lines of ^{12}CO in NGC 7217 using the IRAM Plateau de Bure interferometer (PdBI) in January 2001 (C and D configurations) and January 2003 (B configuration). The six 15 m antennae were equipped with dual-band SIS receivers yielding SSB receiver temperatures around 40 K and 50 K at the two observed frequencies. The system temperatures were 300 K for CO(1–0) and 400 K for CO(2–1). The spectral correlators were centered at 114.906 GHz and 229.808 GHz respectively (i.e., the transition rest frequency corrected for the galaxy's assumed redshift derived from $V_{\rm LSR}$ = 952 km s^{-1}), with three correlator units covering a total bandwidth of 400 MHz at each frequency. The difference between LSR and heliocentric velocities is 12 km s^{-1}, and therefore the observations were centered on $V_{\rm hel}$ = 940 km s^{-1}. The units (each, 160 MHz wide) provided a nominal frequency resolution of 1.25 MHz (3.25 km s^{-1} and 1.62 km s^{-1} for the CO(1–0) and CO(2–1) lines, respectively). The correlator was regularly calibrated by a noise source inserted in the IF system.

Visibilities were obtained with twenty one-minute integrations on the source framed by short (∼2 min) phase and amplitude calibrations on the nearby quasars 2201+315 and 2234+282. The data were phase calibrated in the antenna-based mode. On average, the residual atmospheric phase jitter was less than 30° at both frequencies, consistent with a seeing disk of 0.6″–0.8″ size and with a ∼5% loss of efficiency. The fluxes of the primary calibrators were determined from IRAM measurements and taken as an input to derive the absolute flux density scales for our visibilities, estimated to be accurate to 10%. The bandpass calibration was carried out using 3C273 and is accurate to better than 5%.

The data reduction was performed using the GILDAS software. Data cubes with 512 × 512 spatial pixels (0.25″/pixel) were created with velocity planes distant by 5 km s^{-1}. The cubes were cleaned with the Clark (1980) method and restored by a 2.4″ × 1.9″ Gaussian beam (with PA = 48°) at 115 GHz and 1.2″ × 0.8″ (with PA = 54°) at 230 GHz. The rms noise levels in the cleaned maps (at 5 km s^{-1} velocity resolution) are 3 mJy/beam, and 6 mJy/beam for the CO(1–0) and CO(2–1) lines respectively. No continuum emission was detected toward NGC 7217, down to rms noise levels of 0.2 mJy/beam and 0.45 mJy/beam in a 580 MHz bandwidth at 115 GHz and 230 GHz respectively. The conversion factors between specific intensity and brightness temperature are 16.7 K/(Jy/beam) at 115 GHz, and 15.6 K/(Jy/beam) at 230 GHz. The maps are corrected for primary beam attenuation.

2.3. Images at other wavelengths

We acquired from the HST archive four broadband images of NGC 7217, including WFPC2 (PI: Smartt; PID = 9042) F606W (∼V), F814W (∼I), and NICMOS (PI: Stiavelli; PID = 7331) F110W (∼J), F160W (∼H) data. The optical images were combined with elimination of cosmic rays (*crreject*), and calibrated according to Holtzman et al. (1995). Sky values were assumed to be zero since the galaxy filled the WFPC2 frame, an assumption which at most makes an error of ∼0.1 mag at the corners of the images. The NICMOS images were re-reduced using the best calibration files and were subjected to the van der Marel algorithm to remove the "pedestal" effect (see Böker et al. 1999). Hereafter these F160W images will be referred to as H. All images were rotated to canonical orientation (North up, East left) using the rotation angles provided in the headers.

Optical and NIR surface-brightness cuts of NGC 7217 were derived along the major (PA = 95°) and minor (PA = 5°) axes with a 1″ width, and combined for colors after rebinning onto a common 0.1″ pixel scale. Optical-NIR ($V - H$, $I - H$) color images were obtained by subtracting the magnitude images, after rebinning the higher-resolution NICMOS images to the 0.1″ WFPC2 resolution, and aligning them on the galaxy nucleus. Colors were corrected for Galactic extinction using A_B = 0.38 (Schlegel et al. 1998), and the extinction curve of Cardelli et al. (1989). These data will be discussed in Sect. 5.

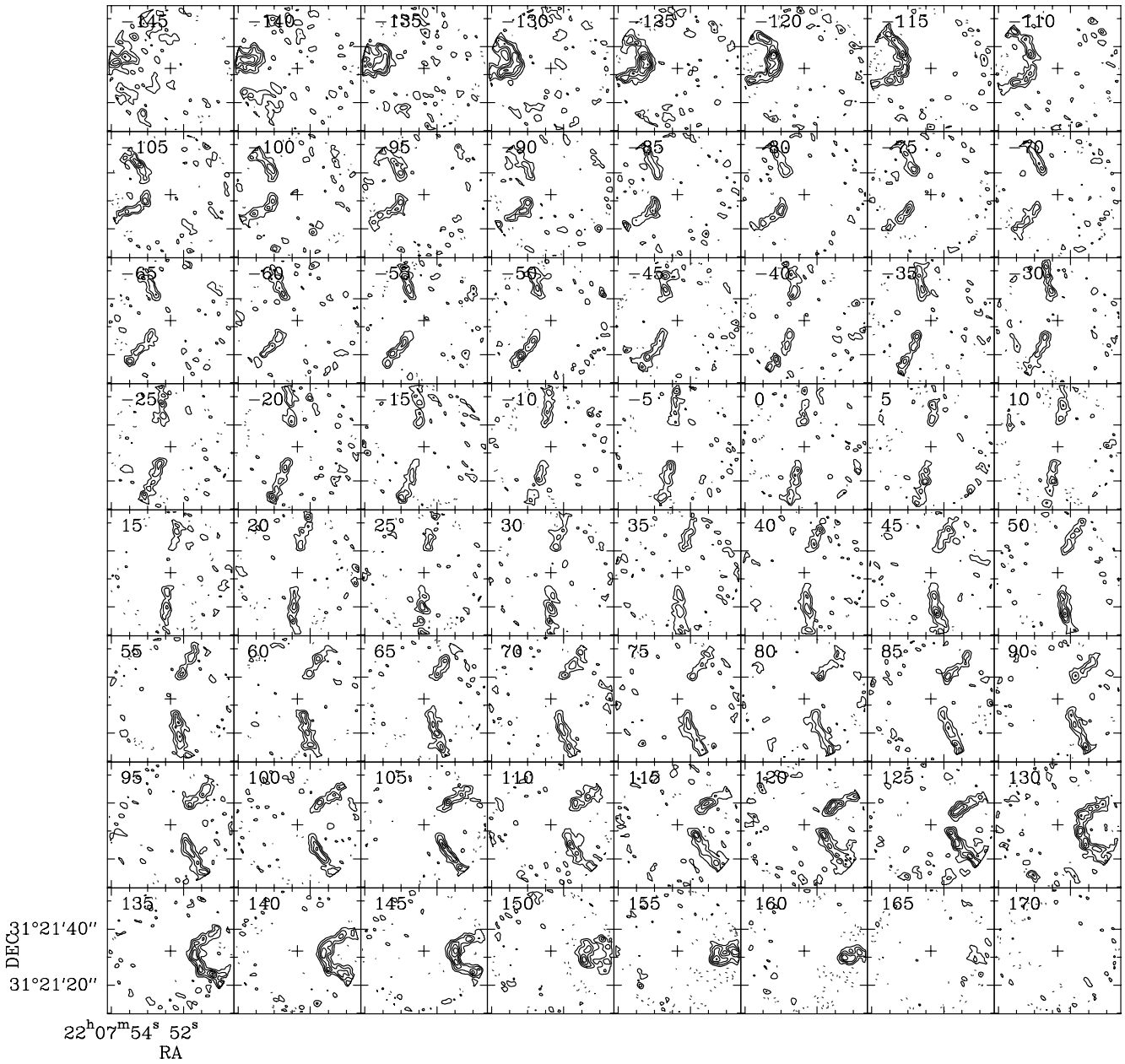

Fig. 1. CO(1–0) velocity-channel maps observed with the IRAM interferometer in the nucleus of NGC 7217 with a spatial resolution of (HPBW) 2.4″ × 1.9″ (PA = 48°). The center of observations, given in Table 1, is indicated by a cross at $\alpha_{J2000} = 22^h07^m52.4^s$, $\delta_{J2000} = 31°21'32.2''$. Velocity-channels range from $v = -145$ km s^{-1} to $v = 170$ km s^{-1} in steps of 5 km s^{-1} relative to $V = 952$ km s^{-1} LSR (or 940 km s^{-1} hel). The maps are corrected for primary beam attenuation. The contours begin at 10 mJy/beam, their spacing is 10 mJy/beam, and the maximum is 50 mJy/beam.

3. Molecular gas results

Figure 1 displays 64 of the channel maps in the CO(1–0) line, with a velocity range of 320 km s^{-1}, and a velocity resolution of 5 km s^{-1}. The velocity field is strikingly regular, showing a classical spider diagram in the iso-velocity contours (see also Fig. 6).

3.1. Morphology of the CO ring

The CO(1–0) integrated intensity distribution, displayed in Fig. 3, reveals a relatively regular and complete ring, with a mean diameter of 25″. The depleted region in the center is striking, as is the steep gradient of emission at the transition of the inside of the nuclear ring (see the radial profile in Fig. 4). The decrease of the emission is much smoother toward the outer edge of the ring. Although complete, the ring consists of individual giant molecular cloud complexes, each with a few 10^6 to 10^7 $M_\odot$, like pearls on a string. The ring is also asymmetric, appearing wider to the South.

Contrary to CO(1–0), the CO(2–1) integrated emission is detected mainly inside the ring, as shown in Fig. 5. The maximum of the emission is in the center, but the nuclear ring itself is quite weak, and certainly suffers from the primary-beam

Table 1. Parameters for NGC 7217.

Parameter	Value	Reference
RA (J2000)	$22^h07^m52.4^s$	NED
DEC (J2000)	31°21′32.2″	center
V_{hel}	952 km s^{-1}	B95
RC3 Type	(R) SA (r) ab	deV
Refined type	(R') SA (rs, nr)ab	B95
Inclination	36°	LEDA
Position angle	95°	LEDA
Distance	14.5 Mpc (1″ = 70 pc)	B95
M(HI)	0.58×10^9 $M_\odot$	B95
L_B	1.6×10^{10} $L_\odot$	LEDA
$L_{FIR}(40-120\,\mu m)$	3×10^9 $L_\odot$	IRAS

B95: Buta et al. (1995).
deV: de Vaucouleurs et al. 1991.

tapering off at a HPBW of 22″, as the CO ring is 25″ in diameter. When the data are tapered in order to lower the resolution and increase the brightness sensitivity, the CO(2–1) ring is better delineated, as shown in Fig. 8.

The mass of molecular gas in the nuclear ring from the CO(1–0) integrated emission is estimated to be:

$$M_{H2} = 3.2 \times 10^8\ M_\odot$$

with the standard conversion ratio of $N(H_2)/I(CO) = 2.2 \times 10^{20}$ cm^{-2} (K km s^{-1})$^{-1}$ (Solomon & Barrett 1991).

The detection of CO(2–1) inside the ring, with a corresponding weak CO(1–0) emission at the center (compatible with a CO(2–1)/CO(1–0) line ratio of 1), implies a mass of $M_{H2} = 4.5 \times 10^5\ M_\odot$ inside $r < 100$ pc (the central beam); this is not a massive molecular disk around the nucleus, but an amount of gas equivalent to a single Giant Molecular Cloud. The central CO(2–1) (and weak CO(1–0)) peak agree with the geometrical center of the CO ring, and with the dynamical center of the CO ring.

3.2. Kinematics of the CO ring

Remarkably, there are no streaming motions or irregularities in the velocity field, in accordance with the very regular and circular nuclear ring. Isovelocity curves of the CO(1–0) emission are superposed on the CO emission in Fig. 6.

The position-velocity diagram along the major axis of the galaxy is presented in Fig. 7. This shows the regularity of the kinematics, and the sharp decline of emission inside the nuclear ring. This confirms the conclusion of B95 that the *flocculent spiral structure* seen in optical images (see Fig. 11) is *trailing*, since the north side is determined to be the near side, given the asymmetry in dust obscuration (see Fig. 11).

3.3. The excitation of the gas

Comparison of the two CO line maps, at the same resolution, and with the same spatial frequency sampling, can yield information about the excitation condition of the gas. We have apodised the CO(2–1) data to sample the same regions of the Fourier plane and give the same spatial resolution at both frequencies. The result is shown in Fig. 8.

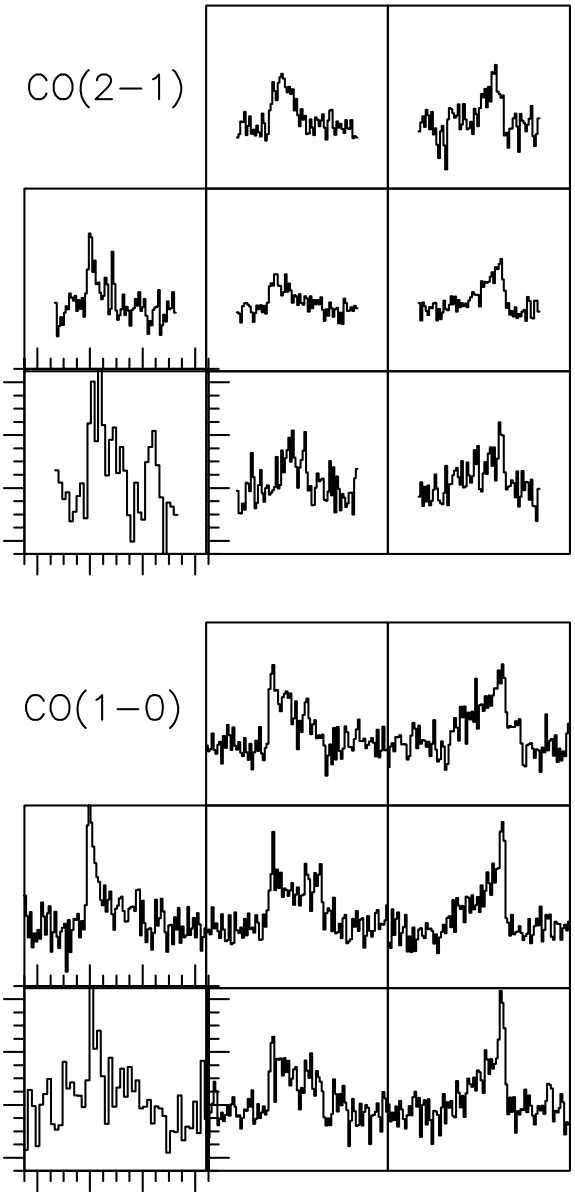

Fig. 2. Small maps of NGC 7217 made with the IRAM 30 m, with 7″ spacing, in CO(1–0) (bottom) and CO(2–1) (top). The velocity scale is −500 to 500 km s^{-1} relative to $V = 952$ km s^{-1} LSR; the T_A^* temperature scale is from −.05 to 0.1 K (or T_{mb} from −.063 to 0.126 K for CO(1–0), and T_{mb} from −.088 to 0.175 K for CO(2–1)). Lack of time prevented to complete the raster in the NE position, but this does not significantly perturb the short-spacing correction.

The CO(2–1)/CO(1–0) ratio is consistent with unity in most of the clumps, although with some scatter (see Fig. 9). Even the maximum of 1.4 (in one of the clumps in the ring) is certainly compatible with optically thick emission, given the uncertainties. The region of the molecular ring is indeed very noisy in the CO(2–1) map after correction for primary beam attenuation, since the ring is in the region where the noise is a factor of two larger than that in the center. This elevated noise might also affect the positions of the CO(2–1) clumps relative to those of the CO(1–0) ones.

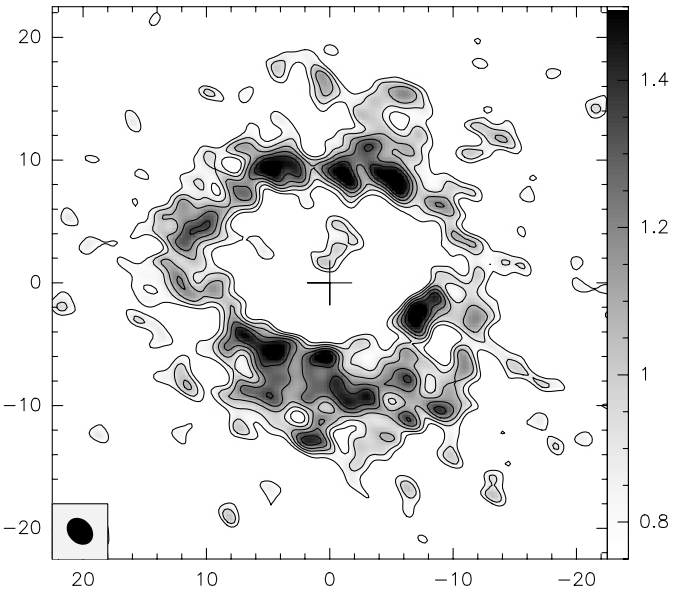

Fig. 3. CO(1–0) integrated intensity contours observed with the IRAM interferometer toward the center of NGC 7217 (the cross marks the coordinates of the center as given in Table 1, with offsets in arcseconds). The map has not been corrected for primary beam attenuation. The rms noise level is $\sigma = 0.15$ Jy/beam km s^{-1}. Contour levels are from 5σ to 10σ with 1σ spacing. The beam of $2.4'' \times 1.9''$ is plotted at the bottom left.

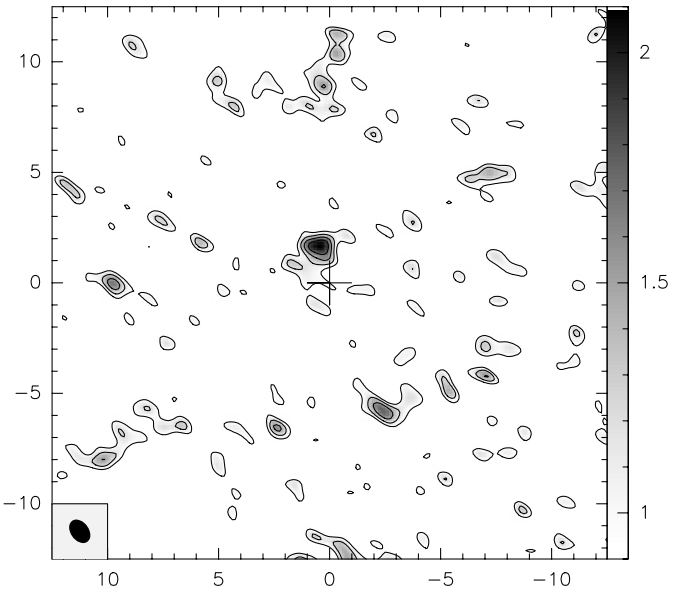

Fig. 5. CO(2–1) integrated intensity map observed with the PdBI toward the center of NGC 7217 (the cross marks the coordinates of the center as given in Table 1, with offsets in arcseconds). The central CO(2–1) emission clump coincides with the actual galaxy center. The map has not been corrected for primary beam attenuation. The noise level is 0.3 Jy/beam km s^{-1}. Contours are from 3σ to 10σ, with 1σ spacing. The beam of $1.2'' \times 0.8''$ is plotted at the bottom left.

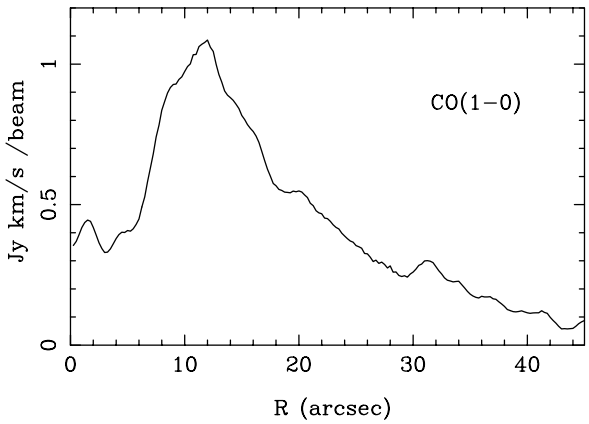

Fig. 4. Radial distribution (azimuthal average, deprojected to face-on orientation) of the CO(1–0) integrated intensity, shown in Fig. 3. This shows the abrupt drop in intensity at the inner edge of the ring.

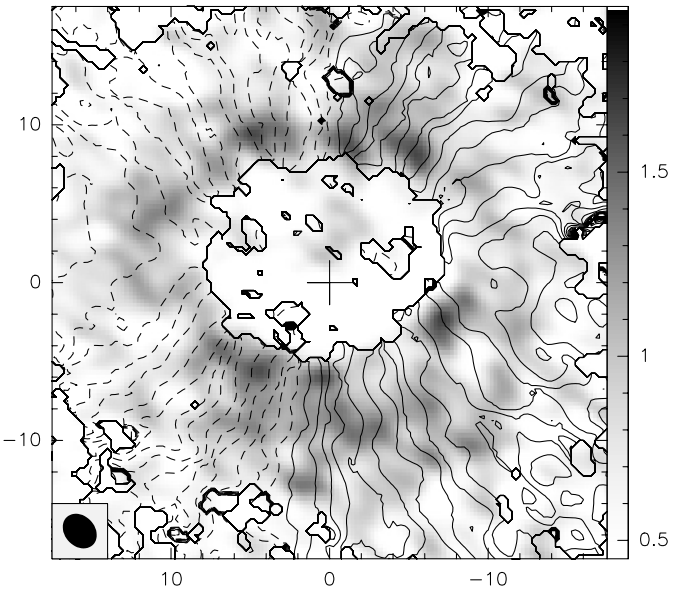

Fig. 6. Overlay of the integrated intensity map of CO(1–0) (in gray scale) with the CO mean-velocity field, in contours spanning the range −150 km s^{-1} to 150 km s^{-1} in steps of 10 km s^{-1}. Velocities are referred to $V_{\rm hel} = 952$ km s^{-1}. Solid (dashed) lines are used for positive (negative) velocities. The first solid contour represents systemic velocity.

3.4. The central CO peak

The CO(2–1) emission peaks toward the center. The spectrum in this region is shown in Fig. 10. The emission is spatially unresolved and corresponds to the tentative detection of a compact disk inside $r = 2''$. There is also a weak CO(1–0) counterpart. As mentioned in Sect. 3.1 however, the molecular mass included in this central spot is only that of one GMC ($4.5 \times 10^5\ M_\odot$).

There may be a link between the circumnuclear ionized gas and our detection of a compact CO(2–1) source. Sil'chenko & Afanasiev (2000) claimed to detect a very central polar ring structure in ionized gas roughly aligned in North-South direction. Their claim of a polar geometry rests on the twisted isovelocity curves in the center. However, this kind of S-shape in the isovelocity curves is rather common in galactic nuclei, and is generally due to non-circular orbits along a bar or spiral arms. Only weak CO(1–0) emission is detected inside the nuclear ring; the present molecular observations do not provide evidence of abundant AGN fueling at the 100 pc scale in

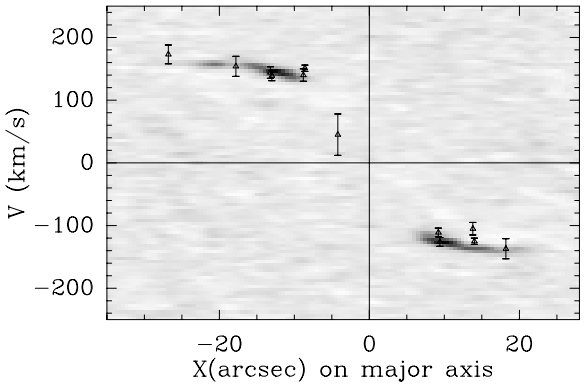

Fig. 7. CO(1–0) position-velocity ($p-v$) diagram along the major axis of NGC 7217 (East is to the right). The center is that of Table 1, and the velocity is relative to $V = 952$ km s^{-1} LSR (or 940 km s^{-1} hel). The markers with error bars show the Hα radial velocities observed by **B95**.

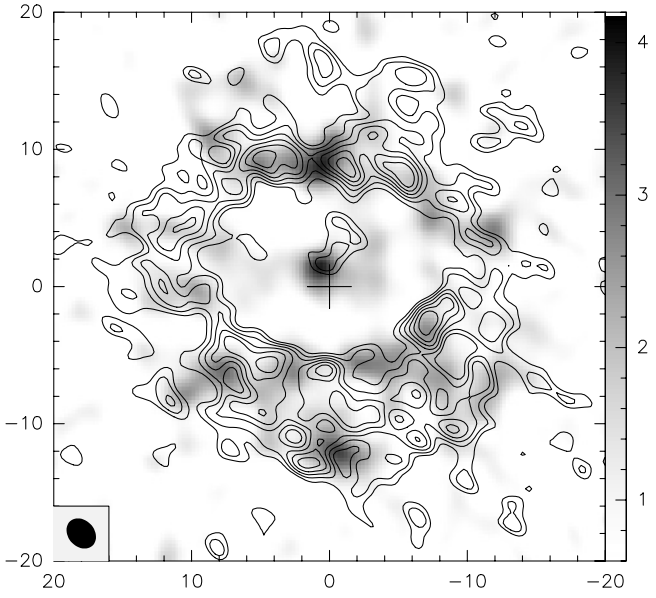

Fig. 8. Contours of the CO(1–0) map (same as Fig. 3), superposed with the greyscale CO(2–1) map tapered and convolved to identical resolution and corrected for primary beam attenuation, in Jy/beam km s^{-1}.

NGC 7217 at present. Some estimate of the accretion luminosity (from the Hα line flux, cf. Ho et al. 1997) indicates that fueling was effective in a recent past.

4. Comparison to other wavelengths

It is of interest to compare the position, size, and symmetry of the CO nuclear ring with those delineated by tracers at other wavelengths (cf. Table 2). Previous ground-based observations revealed, in addition to a blue outer ring at a radius of ∼77″ and a blue inner ring of radius ∼32″, a series of *circumnuclear rings* (CNRs):

1. a red ring at radius ∼14″ (denoted as "inner red ring" by Verdes-Montenegro et al. 1995);
2. a mildly blue (in $V-I$) stellar ring at radius ∼11″ (B95, Verdes-Montenegro et al. 1995);

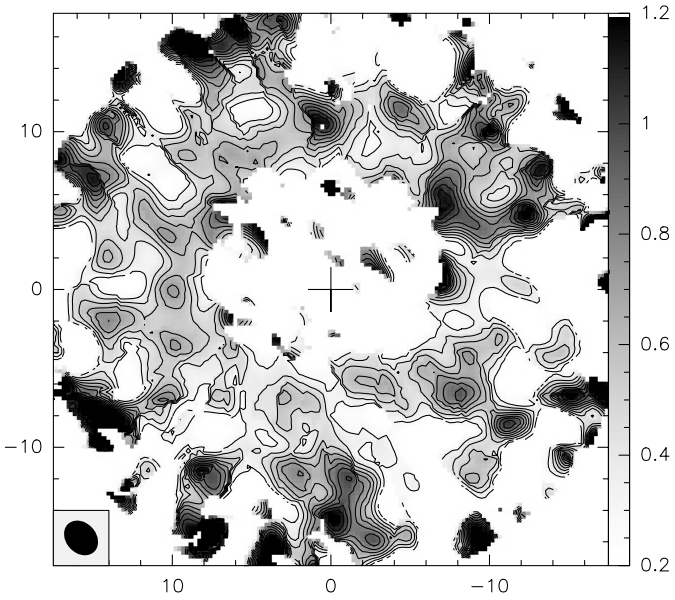

Fig. 9. Contours and grey-scale of the CO(2–1)/CO(1–0) ratio map. The ratio is estimated only when the signals are larger than 3σ. Contours are from 0.2 to 1.2 by 0.1.

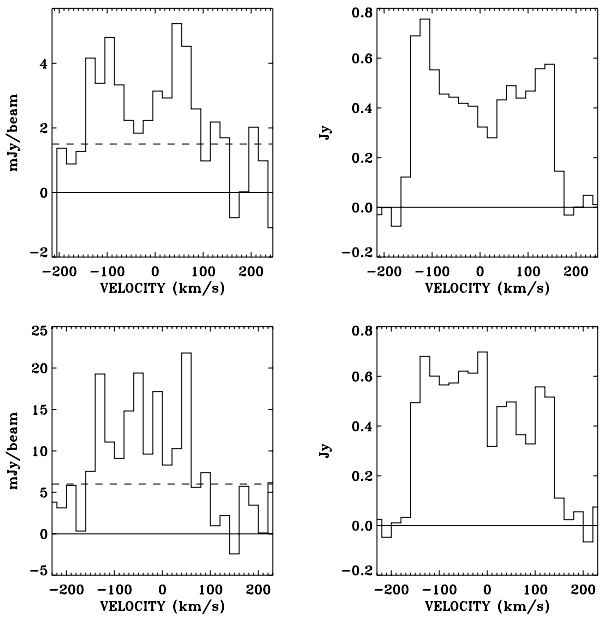

Fig. 10. Left: average CO spectra in the region of maximum emission in the center, covering a 2.4″×1.9″ beam. **top:** CO(1–0), and **bottom:** CO(2–1). The dashed line indicates the 1σ level. **Right:** the spectra summed over the entire CO ring (excluding the center), **top:** CO(1–0), and **bottom:** CO(2–1).

3. an Hα ring (Pogge 1989) coincident with the blue stellar ring; and
4. a red $V-I$ dust ring at a radius of ∼8.6″ (denoted as "nuclear dust ring" by B95).

The "inner red ring", at radius ∼14″, is relatively broad (210 pc, ∼3″) and incomplete, is defined by flocculent spiral structure, and appears as a semi-circle with no red emission to the South; it will be referred to hereafter as the "pseudo CNR". In contrast, the better defined narrower (≤70 pc, 1″)

Table 2. Different rings in NGC 7217.

Parameter	Value	Reference
Radius of outer ring	77″ = 5.4 kpc	B95
Radius of inner ring	32″ = 2.2 kpc	B95
Radius of red ring	14″ = 0.98 kpc	V95
Mean radius of CO ring	12.5″ = 0.9 kpc	this work
Stellar nuclear ring	10.7″ = 0.75 kpc	B95
Hα nuclear ring radius	10.7″ = 0.75 kpc	P89
Dust ring ($V-I$)	8.6″ = 0.6 kpc	B95

B95: Buta et al. (1995).
V95: Verdes-Montenegro et al. (1995).
P89: Pogge 1989, and also Verdes-Montenegro et al. (1995).

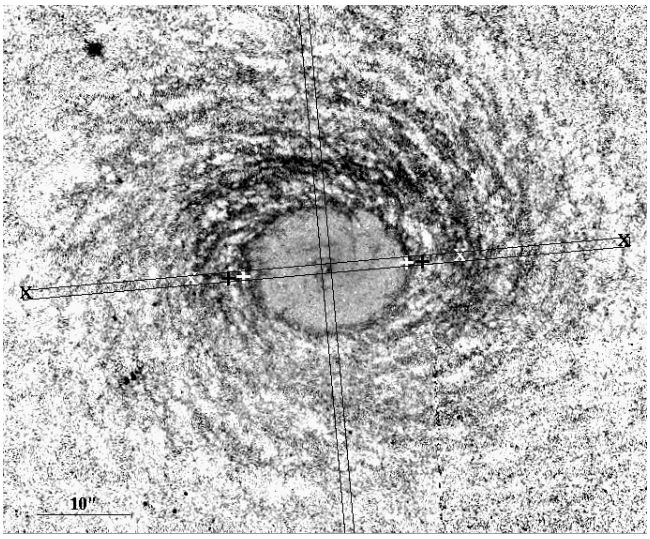

Fig. 11. HST $V-I$ (transformed from F606W-F814W) image with major- and minor-axis cuts superimposed. The positions of the rings are shown as a *i)* white cross = red dust CNR; *ii)* black cross = blue stellar CNR, Hα ring; *iii)* white × = pseudo CNR; *iv)* black × = blue stellar inner ring. Darker pixels correspond to redder colors, and lighter pixels to bluer. The total horizontal size of this image is 67″ (North is up and East is left). Same color scale as in Fig. 12.

circumnuclear red dust ring at radius ∼8.6″ forms a closed oval structure, as do the slightly larger stellar and Hα rings. Figure 11 shows the positions of these rings in cuts superimposed on the HST $V-I$ image; the cuts will be described in Sect. 4.3. Our HST $V-I$ image clearly resolves all the rings, and reveals additional substructure (e.g., blue star clusters) which was previously not obvious from ground-based images.

4.1. Circumnuclear rings

Figure 12 shows the superposition of the CO(1–0) contours onto the HST $V-I$ map. $V-I$ essentially traces extinction but blue colors of young stars can also be seen just outside the red dust CNR. The molecular ring starts abruptly at exactly the position of the inner well-defined dusty CNR (radius 8.6″, see also Fig. 4), and covers the stellar and ionized gas CNRs, out to the flocculent trailing spiral structure in the pseudo CNR.

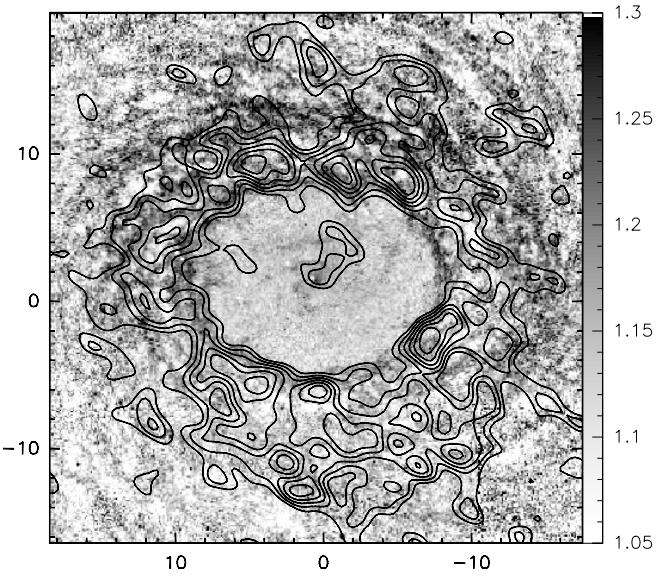

Fig. 12. CO(1–0) low-resolution contours superposed on the HST $V-I$ color image. Darker pixels correspond to redder colors, and lighter pixels to bluer.

The bulk of the CO(1–0) molecular ring is coincident with, although broader than, the CNRs revealed by other tracers. Indeed the CO(1–0) integrated intensity map shows a ring significantly broader than either the dust or stellar CNRs. If fitted by a Gaussian, the half-power width is of order 570 pc (∼8″); measuring the half-power width directly gives an even larger value, closer to 700 pc (∼10″) (see Fig. 4). The CO resolution is not sufficient to separate the nuclear ring itself from the pseudo CNR and flocculent spiral structure that blends with it at larger radii. The sharp cutoff of the CO ring is conspicuous on its inner edge, but then the ring merges with the spiral structure outside, visible in the dusty flocculent features, and well resolved by the HST color image.

4.2. Nuclear spiral and blue nucleus

At the center of the galaxy and its CNR, there is a small multi-arm spiral dust lane encircled by the larger flocculent one. Figure 13 shows the superposition of the CO(2–1) contours on the HST $V-I$ map. The CO(2–1) contours in the very center coincide with the dusty mini-spiral delineated by the red colors in the HST $V-I$.

The nucleus turns out to be rather blue in $V-I$ ($V-I=1.2$), ≳0.3 mag *bluer* than a red knot ($V-I=1.5$) to the southwest. Figure 14 shows a close-up of the center of NGC 7217 in $V-I$; the position of the continuum peak is shown as an open square. This red knot appears to be the center of the nuclear spiral, which also has red colors (although 0.1–0.15 mag bluer than those of the knot) and appears to be dusty. The blue nucleus and the red knot are separated by roughly 0.3″, or ≈24 pc. The blue colors of the nucleus subtend a region of 28 pc × 20 pc, with a position angle of ∼30°.

The presence of gas and dust in a spiral structure inside the nuclear ring suggests that some gas is still able to make its way

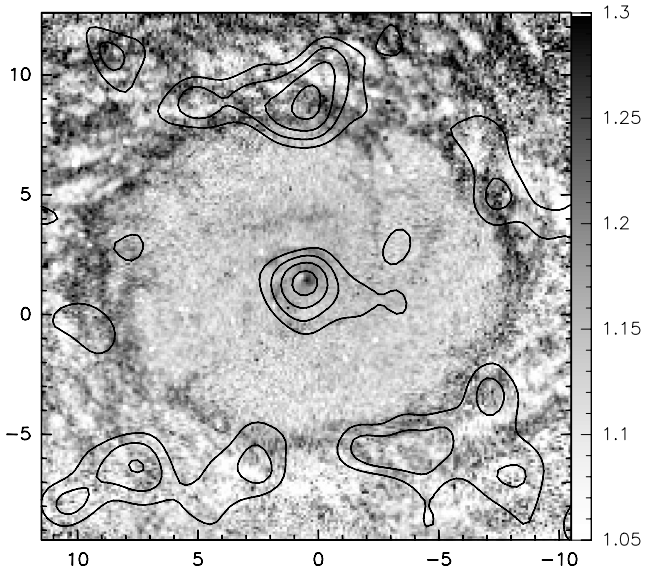

Fig. 13. CO(2–1) contours superposed on the HST $V - I$ color image. As in Fig. 12, darker pixels mean redder colors. The CO(2–1) peaks exactly at the center of the nuclear bar/spiral feature.

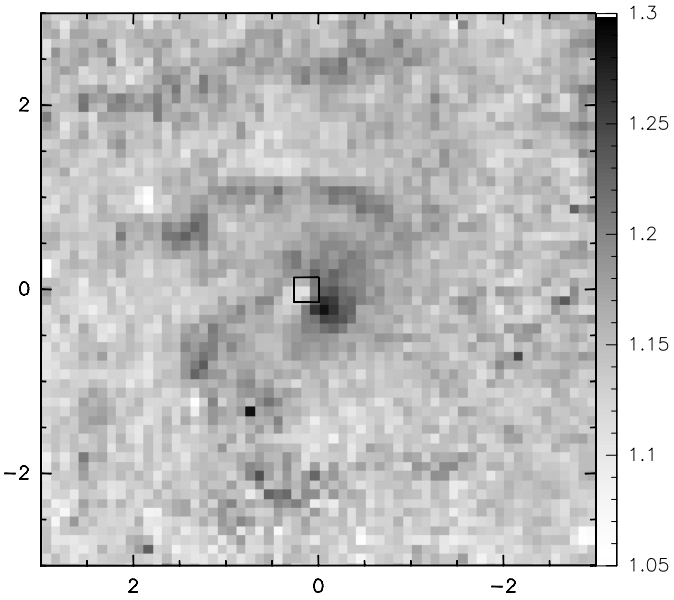

Fig. 14. Zoomed $V - I$ image of center of NGC 7217 with continuum brightness peak (in both F606W and F814W) indicated with an open square. Darker pixels correspond to redder colors, and lighter to bluer ones. Axes are in arcsec. The center (0, 0) is now the galaxy center.

towards the nucleus through viscosity, in spite of the opposing action of the gravity torques.

4.3. North-south asymmetry

As mentioned previously, the broad CO ring is roughly coincident with the narrow stellar and Hα ring at ~11″. The CO(1–0) emission starts just on the red dust ring at a radius of 8.6″; and is very broad, almost ten times wider than the red dust or stellar rings. Interestingly, while the stellar and red dust rings are closed structures, the pseudo CNR just outside the stellar

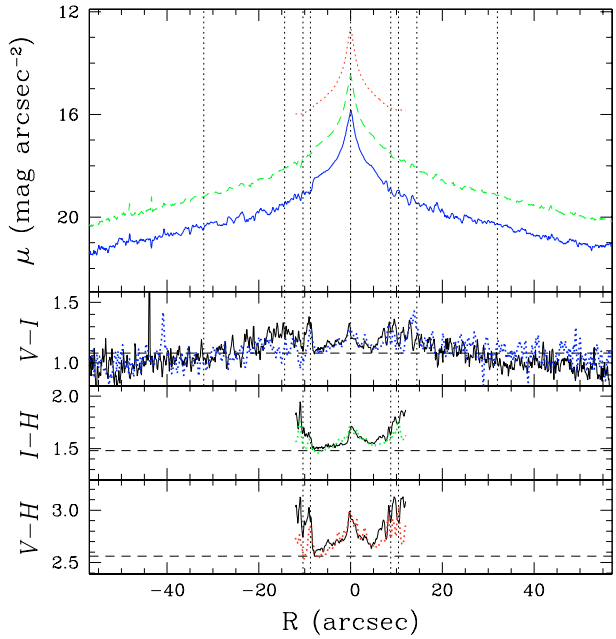

Fig. 15. Surface brightness cuts taken along the slits shown in Fig. 11. The dotted line corresponds to F160W, the dashed line to I, and the solid line to V. In all panels, the various ring positions are shown by vertical dotted lines (from center: red dust ring, stellar ring, pseudo CNR, and inner stellar ring). In the lower panels, major-axis cuts are shown as solid lines and minor-axis cuts as dotted lines; horizontal dashed lines illustrate the colors of a 26 Myr stellar population reddened by 1.1 mag of extinction (see Sect. 5). The minor-axis cuts have been rectified by using an axial ratio of 0.8.

ring appears as a semi-circle, open in the direction where CO is broader. The implication is that the asymmetry of the red pseudo CNR cannot be ascribed to an intrinsic hole in the dust, since the CO emission is on the contrary even more conspicuous toward the south.

The north-south (N-S) asymmetry can be seen more clearly in Fig. 15, which shows major- and minor-axes cuts and their colors, taken at the positions shown in Fig. 11. In the figure, dotted curves show the minor-axis cuts rectified to circular shapes (inclination = 36°; PA = 95°). Also shown as vertical dotted lines are the positions of the various rings. Inspection of the figure shows clearly the effect of the flocculence on the colors (ripples in the color curves) and that the $V - I$ color (see short-dashed profile) is significantly bluer toward the S (negative galactocentric distance) than toward the N at the position of the pseudo CNR at ~14″. Paradoxically, it is toward the South, suffering less extinction, that the CO emission is stronger, and the molecular ring more massive.

The reasons for such a north/south asymmetry are not clear, but perhaps the flocculent spiral structure widens the CO nuclear ring, which is more conspicuously stochastic in the south.

5. Circumnuclear star formation

5.1. Colors, ages and extinction

To better characterize the star formation history and the ages of the stellar populations in NGC 7217, we have measured the

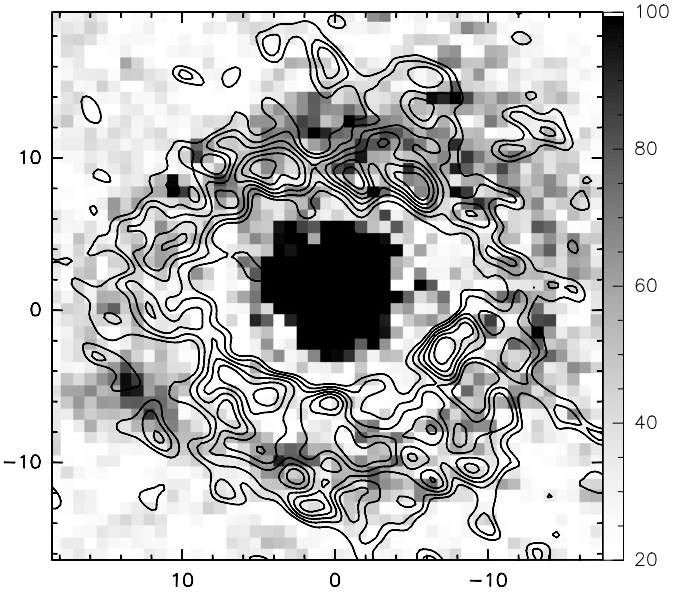

Fig. 16. Contours of CO(1–0) emission (same as Fig. 3), superposed on the continuum subtracted Hα+[NII] gray-scale map from Pogge (1989). Offsets are in arcseconds.

$V-I$, $I-H$, and $V-H$ colors of several circumnuclear regions: the "red knot" in the nuclear spiral, the (blue) nucleus, the region inside the dust CNR, the dust CNR itself, and the blue stellar ring.

We have performed a least-square fit of the colors for each region to the solar metallicity evolutionary synthesis models by Leitherer et al. (1999, hereafter SB99, dealing with a single burst and Salpeter IMF).

We conclude that the blue nuclear stellar ring and the regions encircled by it are dominated by relatively young stellar populations (10–50 Myr), with varying amounts of extinction ($A_V \sim 1-2$ mag). These are not typical features of early-type spiral galaxies, and are probably the result of a significant gas reservoir and the ensuing massive star formation. Indeed, ionized gas emission, traced by the gray-scale Hα map underneath the CO(1–0) contours in Fig. 16, shows that star formation is still occurring in the nuclear regions (nucleus, red knot, multi-armed spiral), and in the CO ring (although there is in the center the contribution of the AGN). The ionized gas traces very well the blue stellar ring, but is absent in the red dust CNR, probably because of the large extinction there. However, observations of recombination lines at longer wavelengths are needed to better quantify the dust distribution, and hence to confirm our previous conclusion.

5.2. The nature of the nuclear spiral

The nuclear multi-armed spiral in NGC 7217 revealed by the HST images is similar to those in other early-type flocculent galaxies (e.g. Martini et al. 2003). It is not an obvious continuation of the structure outside the CNR, which if it corresponds to an inner Lindblad resonance (ILR), should shield the nuclear region from incoming spiral waves (Bertin et al. 1989). However, it is affected by $\gtrsim$1 mag of dust extinction, and its colors suggest that it hosts a recent (20−40 Myr old) starburst. In other flocculent galaxies (Elmegreen et al. 1998, 2002), such small-scale spiral structure has been attributed to acoustic turbulence and implicated in the fueling of the LINER activity. Such spiral pieces could only be material arms, e.g. giant molecular clouds, sheared off by differential rotation.

Following Thornley (1996), we have measured the ratio of the nuclear spiral arms in the I and H bands relative to a symmetric model. The nuclear spiral in the NICMOS F160W appears in an unsharp-masking image, although with very weak amplitudes, ranging from 1.01 to 1.05. The I band shows similarly small excursions. Since near-infrared amplitudes of typical density-wave spirals range from 1.5 to ∼3.0 (e.g., Rix & Zaritsky 1995), we conclude that the nuclear spiral in NGC 7217 cannot be a stellar density wave. The presence of gas and dust in this feature may show how gas is brought to the nucleus.

6. Dynamical model of the galaxy

6.1. Overview

To summarize the essential features found in the previous sections, the molecular gas in NGC 7217 has a very regular morphology and is concentrated in a nuclear ring. This ring's most striking feature is its extremely sharp inner edge. When the molecular gas distribution is compared to the HST $V-I$ image, it becomes clear that the broad CO distribution is composed of a narrow ring, coincident with the stellar and Hα nuclear ring of 1.5 kpc diameter, and a broader "ring" of flocculent spiral arms extending to larger radii, with a width of ∼400 pc. This complexity explains the apparent radial shift of average ring radii among the various components, as noted in Table 2. The CO ring and spiral arms are very clumpy, with dense gas in giant molecular complexes (with a few 10^6 to 10^7 $M_\odot$).

There is a mini spiral structure inside the ring, gaseous and dusty, which contains only a very small amount of gas (of order 5×10^5 $M_\odot$). With this small mass spread over a relatively large area (i.e. surface density of the order of 0.3 $M_\odot$/pc^2), it is likely that this structure is not a single self-gravitating unit. At 1 kpc radius, the Toomre critical surface density for axisymmetric instabilities is about 300 $M_\odot$/pc^2; inside the ring, however, the average molecular surface density is 1 $M_\odot$/pc^2 (individual clouds can still be self-gravitating). This gas could flow inward very slowly due to viscous torques.

The most likely interpretation of the global structure is in terms of resonant rings produced by a bar structure that has faded into an oval distortion by now (e.g. B95). Even the slight oval observed today is able to form the observed rings, as shown by the simulations of gas flow in the potential derived from a red image (B95). The main gravity torques inside the nuclear ring are positive, driving the gas out toward the ring boundary. However, even if there were a bar some time ago, the gravity torques are now weak, and some gas could still flow in through viscous torques, explaining the presence of the multi-armed spiral inside the ring.

Given the weakness of the oval distortion observed now, the abrupt cutoff at the inner edge of the nuclear CO ring is difficult to explain. Two solutions can be considered: either a strong

bar formed the rings in the recent past, and the present morphology shows the residual signatures of that process, or there have been only weak oval distortions recently, one of which is still at play today. We explore these possibilities, with the help of N-body simulations. This self-gravitating model is the next step in the interpretation proposed by B95, who computed only the gas response in a fixed potential, at a fixed time. Our aim here is to find a plausible dynamical scenario to account for the presently observed gravitational potential; this requires that we follow the evolution of all components, including the evolution of the gas content, and therefore star formation and feedback are included. In contrast to B95, we will focus on the central region, where we have many new observational constraints coming from the high-resolution HST images and the interferometric CO data. Only the formation of the nuclear ring is studied, and our examination of the gas is confined to the center. We do not follow the formation of the more external rings, since these would require external gas accretion, that has been ignored here.

6.2. Physical model adopted for the galaxy and numerical techniques

In order to understand the observed morphology, we performed N-body simulations with stars and gas, including star formation. The regularity and axisymmetry of the bulge and stellar halo components led us to consider them as spherical, and rigid potentials, in which the disk component evolves (e.g. Sellwood 1980). Self-gravity is only included for the disk (gas + stars). 2D N-body simulations were carried out using the FFT algorithm to solve the Poisson equation, with a polar grid, to optimize the spatial resolution toward the center.

The polar grid is composed of $NR = 64$ radial, and $NT = 96$ azimuthal separations. While all azimuthal increments are equal, the radial grid is exponential, with the cell size ranging from 17 pc at the center to ~1 kpc at the outskirts (at 15 kpc). The softening is also variable, ranging from 50 pc near the center to 1 kpc. The number of cells is chosen so that cells are approximately square at all radii (almost equal size in radius and azimuth). Radii of the grid points are given by:

$$R_I = 0.25 \exp(2\pi I/NT)$$

for $I = 1$ to 63; and $R_0 = 0$ for $I = 0$. The self-force introduced by the polar grid is subtracted at each time-step, as already described in Combes et al. (1990).

The stellar component is represented by 80 000 particles, and the gas component by 40 000. When an extended bulge component is added, to control the disk stability and the bar strength, it is a rigid spherical potential, with a Plummer shape:

$$\Phi_{\rm EB}(r) = -\frac{GM_{\rm EB}}{\sqrt{r^2 + r_{\rm EB}^2}}$$

for $M_{\rm EB}$ and $r_{\rm EB}$ the mass and characteristic radius of the extended bulge component respectively. To fit the rotation curve of NGC 7217, however, the characteristic radius of this component has to be small, 3.5 kpc. This component may be considered either as the extended bulge or the stellar halo that has been previously noticed in this galaxy (e.g. B95).

Table 3. Initial conditions parameters.

Run	$r_{\rm b}$	$M_{\rm b}$	$M_{\rm d}$	$M_{\rm EB}{}^*$	$F_{\rm gas}$	$f_{\rm el}$
	kpc	$M_\odot$	$M_\odot$	$M_\odot$	%	
Run A	0.5	2.7e10	4.5e10	6.0e10	3	0.35
Run B	0.7	3.6e10	7.0e10	0.	1.5	0.65
Run A1	0.5	2.7e10	4.5e10	6.0e10	6	0.65
Run A2	0.5	2.7e10	4.5e10	6.0e10	1.5	0.35
Run A3	0.6	3.2e10	5.0e10	4.5e10	3	0.65
Run A4	0.7	3.6e10	5.0e10	5.0e10	3	0.35
Run A5	0.8	3.6e10	3.6e10	6.0e10	3	0.65
Run B1	0.5	2.7e10	6.0e10	4.5e10	6.	0.65
Run B2	0.5	2.7e10	6.0e10	4.5e10	3.	0.35
Run B3	0.5	2.7e10	7.7e10	2.7e10	3.	0.35
Run B4	0.5	2.7e10	7.7e10	2.7e10	6.	0.65
Run B5	0.5	2.7e10	1.0e11	0.	6.	0.85

* Extended Bulge (EB) mass inside 14 kpc radius.
$r_{\rm d}$ and $r_{\rm EB}$ are fixed at 3.5 kpc.

The stellar disk is initially a Kuzmin-Toomre disk of surface density

$$\Sigma(r) = \Sigma_0 \left(1 + r^2/r_{\rm d}^2\right)^{-3/2}$$

truncated at 14 kpc, with a mass $M_{\rm d}$. It is initially quite cold, with a Toomre Q parameter of 1. The bulge is a Plummer sphere, with mass $M_{\rm b}$ and characteristic radius $r_{\rm b}$. The time step is 0.1 Myr. The initial conditions of the runs described here are given in Table 3.

The gas is treated as a self-gravitating component in the N-body simulation, and its dissipation is treated by a sticky particle code, as in Combes & Gerin (1985). The initial gas-to-total mass ratio ($F_{\rm gas}$) ranges between 1 and 6%, since the star formation in the simulation is capable of reducing $F_{\rm gas}$ to its observed low value. The mass of one gas particle therefore varied between 4×10^4 and 2×10^5 $M_\odot$. At the present time, the observed gas mass in NGC 7217 is only 0.8×10^9 $M_\odot$, representing about 1% of the total mass inside 10 kpc required to fit the observed rotation curve. The initial distribution of gas in the model is an exponential disk, truncated at 12 kpc, and with a characteristic radial scale of 2 kpc. Initially, its velocity dispersion corresponds to a Toomre Q-parameter of 1. The gas clouds are subject to inelastic collisions, with a collision cell size of 240 pc (region where particles are selected to possibly collide). This corresponds to a lower limit for the average mean free path of clouds between two collisions. The collisions are considered every 5 to 10 Myr. In a collision, the sign of the relative cloud velocities is reversed and the absolute values are reduced: relative velocities after the collision are only $f_{\rm el}$ times their original value, the elasticity factor $f_{\rm el}$ being between 0.35 and 0.85, as indicated in Table 3. The dissipation rate is controlled by this factor. All gas particles have the same mass.

Star formation is taken into account following a generalised Schmidt law: the star formation rate is proportional to the volume density to the power $n = 1.2$, provided that the density is larger than 1 H-atom cm^{-3}, i.e. the rate of gas mass transformed into stars is $\mathrm{d}m = \mathrm{d}tC_*\rho^{1.2}$. To compute this rate, at regular intervals of $\mathrm{d}t = 5-10$ Myr, the gas density is averaged in 240 pc

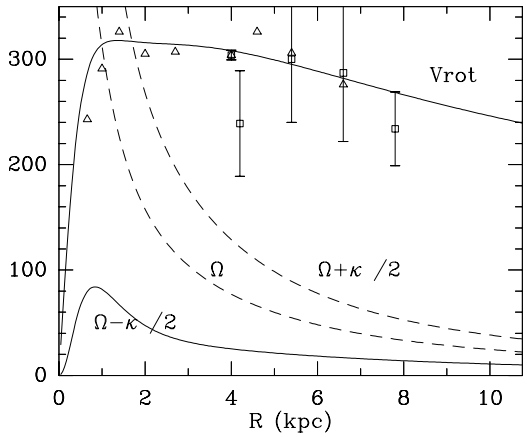

Fig. 17. Rotation curve and derived frequencies Ω, $\Omega - \kappa/2$ and $\Omega + \kappa/2$ adopted for the simulations (Run A). The triangles are the Hα rotational velocities; the squares are from the HI data (see B95).

cells, and the probability of the gas particles being transformed into stars is computed by

$$P = \mathrm{d}m/M_{\mathrm{cell}}$$

for all particles in this cell, of mass M_{cell}. Each new star formed has exactly the same mass as each gas particle, about 5 times smaller than any old stellar particle. This simple scheme corresponds to an instantaneous recycling of matter, since the continuous mass-loss from recently formed stars is not followed. The rate of star formation is normalised so that in unperturbed runs (without galaxy interaction, galaxies are quiescently and regularly forming stars), the timescale for consumption of half of the gas mass is of the order of 2 Gyr (SFR $\sim$ 1–2 $M_{\odot}$/yr). At each star formation event, the neighbouring gas particles are given a small extra velocity dispersion of order $\sim$10 km s^{-1}.

The rotation curve corresponding to one of the runs is plotted in comparison to the data points in Fig. 17. All other runs have similar rotation curves. Given the uncertainties, all curves are compatible with the data.

7. Simulation results

About 50 runs have been carried out to test the various parameters and evaluate the dependence of the results on dissipation rate of the gas, and the initial total mass of the gas. These are crucial in determining the disk stability, and the strength of the developed bar or oval distortion. Only a dozen of these models are displayed in Table 3.

The stellar disk self-gravity is the most essential parameter affecting the stability and bar strength. To restrict the volume of parameter space to explore, we have chosen to fix the scale lengths of the mass components, and mainly vary only the *masses* of two components (the disk and extended bulge). Only two representative runs (A and B), will be discussed here; their mass parameters are displayed in Table 3. These two runs are typical of two categories of models, A*i* leading to weak bars or oval distortions, and B*i* to strong bars.

Run A, with a maximal bulge mass, provides the best fit for NGC 7217. Run B is the maximum disk solution, where there is no extended bulge component. The strength of the $m = 2$ perturbation increases steadily as the mass ratio between disk and bulge is increased. However, for a given mass ratio, the $m = 2$ strength also varies significantly with the initial gas mass (i.e., F_{gas}, the disk being more unstable with larger gas mass fraction), and the dissipation rate, controlled by the elasticity of collisions (f_{el}). The more dissipation, the cooler the disk, the more prominent the bar, and the greater the departure of the gas behaviour from that of the stellar component, with the gas having an increasing tendency to form rings. With less dissipation, the rings are less contrasted, and more of the gas particles share the bar morphology.

Given the present unbarred structure of NGC 7217, there could be two possibilities to account for the present ring morphology. One possibility is that the galaxy was strongly barred in the recent past, that gaseous rings have developed, and that new stars have formed in these rings; then the bar has disappeared, but the rings have remained. This solution requires a large mass of gas, so that the radial gas flow driven by the bar can indeed build a mass concentration of at least 5% of the total mass (Hasan et al. 1993). The other possibility is that the rings have developed through the action of an oval distortion alone, which is still present (B95). This solution has the advantage of explaining the abrupt inner edge of the nuclear ring, since gravity torques would still be present to compensate for the natural tendency of the gas to diffuse and spread radially out of the rings.

To explore this last solution, and to account for only a weak oval distortion in the disk, the disk must not be completely self-gravitating, and a significant part of the mass should exist in the spherical bulge. This corresponds to the initial mass distribution of Run A (Table 3). The rotation curve for this mass distribution is plotted in Fig. 17. The initial gas mass was maximum in this run, $M_{\mathrm{gas}} = 4 \times 10^9\ M_{\odot}$, or 3% of the total mass. The dissipation was also important, with the collision time-scale of 5 Myr, and a collisional rebound coefficient (or elasticity factor) of $f_{\mathrm{el}} = 0.35$. A snapshot of the typical morphology between 1 and 2 Gyr is plotted in Figs. 18 and 19. A very weak bar developed, as shown in Fig. 20, with a high pattern speed, above the maximum of the $\Omega - \kappa/2$ curve (see Fig. 21). Since the mass concentrates as evolution proceeds, the $\Omega - \kappa/2$ curve rises, and there is just one ILR. The nuclear ring falls at the radius of the maximum of the $\Omega - \kappa/2$ curve. For all other runs of this type (Ai in Table 3), the pattern speed is always high, between 100 and 150 km s^{-1}/kpc, and the ILR, the CR, and the OLR resonances are at about 1, 2–3, and 4–5 kpc.

There is very little gas inside the nuclear ring, but still some gas is flowing inward. There could be intermittent instabilities of the very sharp inner edge of the ring, and some gas clouds may flow inwards. These are not part of a wave, but might be sheared into transient material spiral arms through differential rotation inside in the ring. If they have no fixed position with respect to the oval pattern, the torques exerted on them cancel out.

The evolution of the overall circumnuclear star formation rate is indicated in Fig. 22.

At the other extreme, Run B has most of the mass in its self-gravitating stellar disk. It is therefore highly unstable to bar

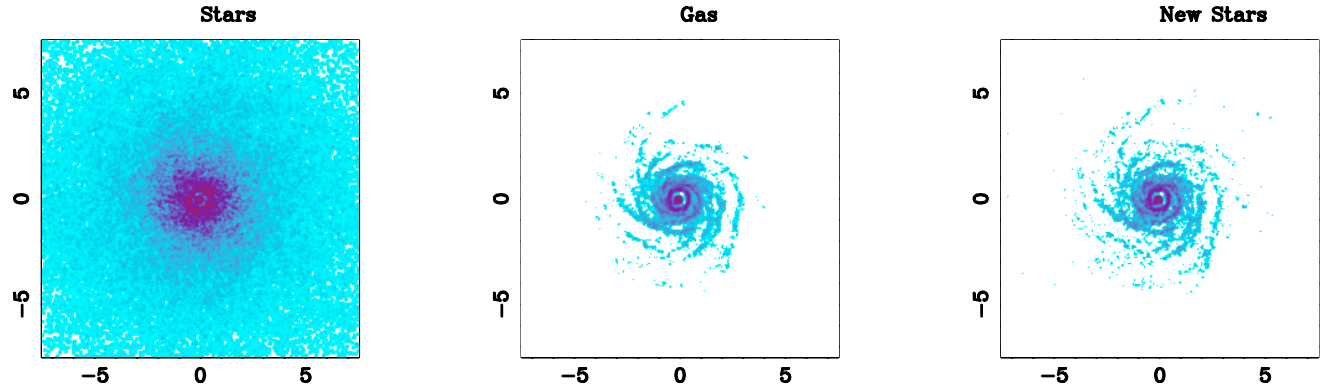

Fig. 18. Left: gray scale plot of the stellar component distribution, in Run A (the gray scale is linear and axes are in kpc). **Middle:** gray scale plot of the corresponding gaseous component (the gray scale is logarithmic). **Right:** plot of the stars formed during the simulation (the gray scale is logarithmic).

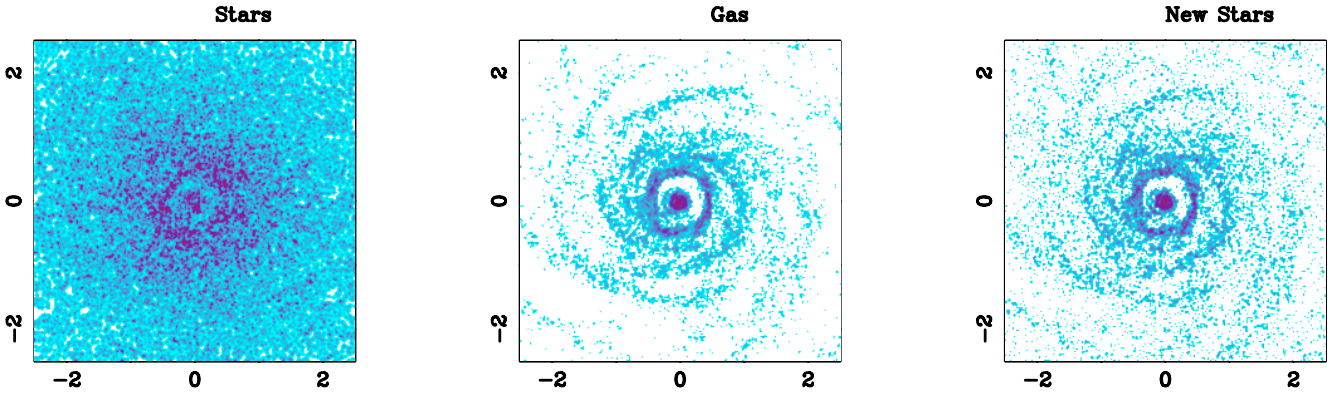

Fig. 19. Same as Fig. 18, but zooming toward the center (the axes are in kpc).

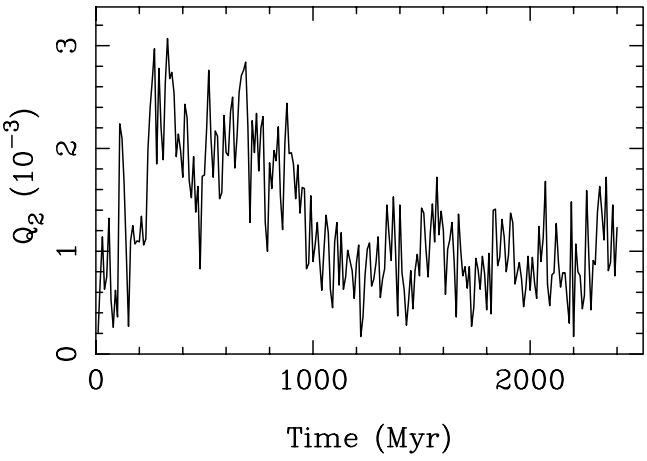

Fig. 20. Evolution of the bar or oval distortion strength in Run A, estimated from the maximum Q_2 over radius of the ratio: $m = 2$ tangential force divided by the radial force.

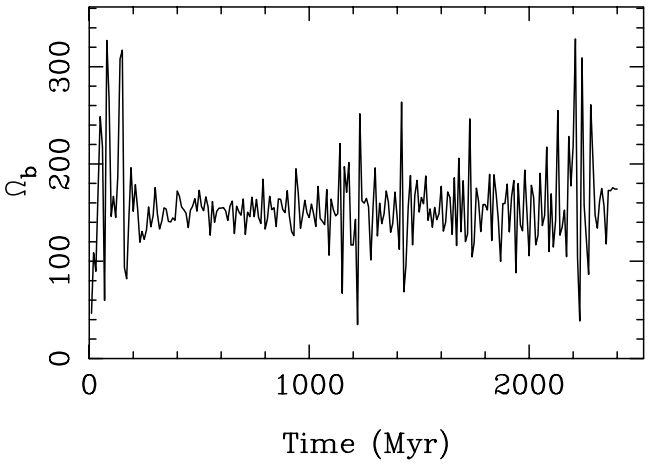

Fig. 21. Evolution in Run A of the pattern speed of the $m = 2$ distortion. Ω_b is estimated from the Fourier transform of the potential every 10 Myr, and in particular the evolution of the $m = 2$ phase.

formation, although the gas mass here is only $M_{gas} = 1.6 \times 10^9\ M_\odot$, ~1.5% of the total. The dissipation was made less important, with the collision time-scale of 10 Myr, and a collisional rebound coefficient of $f_{el} = 0.65$. The resulting morphology between 1 and 2 Gyr, is plotted in Fig. 23.

In this run, the bar is so strong, and the radial gas flow so important that only a small gas fraction remains in the disk at the end. Moreover, the radius of the ring shrinks, and the ring disappears: even if the bar were destroyed later, no ring would survive the bar. However the bar remains, since the gas mass is insufficient to dissolve it via gas infall.

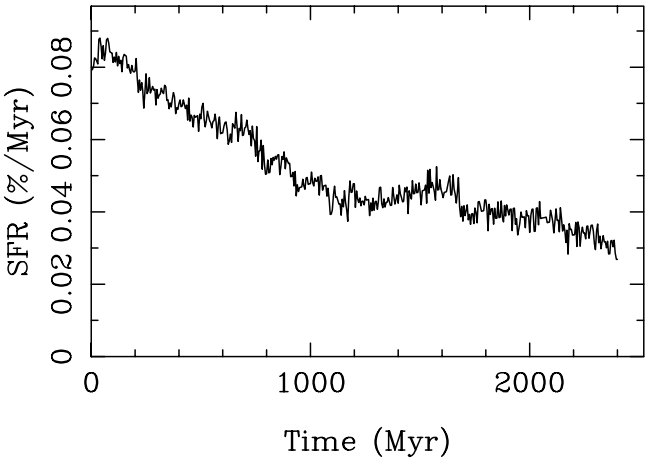

Fig. 22. Star formation rate as a function of time for Run A. It is estimated as the percentage of the gas mass transformed into stars per Myr.

8. Discussion

The results of runs A and B have clarified the possible nature of the present nuclear ring on NGC 7217: the most likely solution is that the ring has been formed by a recent weak oval distortion, which has declined in strength but still plays a role in maintaining the sharp inner boundary of the ring in molecular gas. The galaxy is not likely to have been strongly barred in the recent past (i.e. in the last 700 Myr or so), since the ring would not have formed at its observed location with a circular shape. The massive bulge in this galaxy stabilizes the disk, and supports the weak bar solution. If the galaxy were strongly barred in the past, such a configuration must date back to prior to the building of the extended bulge.

8.1. Other runs

For the sake of simplicity, we have described two models compatible with the observed rotation curve with rather extreme bulge-to-disk mass ratios. However, many other runs with variations of the main parameters were carried out. These experiments have revealed which parameters play the largest role in the dynamics: the disk mass ratio, the gas fraction, and the character of dissipation. All three act on the stability of the disk, but differently. When the disk mass is too dominant, a strong bar develops, but then the gas is driven too fast toward the center, and no ring forms. In the intermediate cases, the remaining gas forms a resonant ring that is too elliptical in shape. When stars form out of this gas, the stellar nuclear ring cannot be made circular enough to comply with the observed morphology. Rings as circular as observed are only found for a very weak bar.

The efficiency of forming a contrasted ring depends mainly on the amount of gas and its dissipation rate. For an almost axisymmetric potential, the gas must be self-gravitating and very cold to react as observed. The absence of strong perturbations then maintains the cold character of the gas component.

Even in the case of the development of a weak bar, the gas disappears progressively because of star formation and slight inflow toward the center; consequently the disk stabilizes and the bar slowly fades away (Fig. 20). There still remains a strong enough perturbation to maintain a positive torque for the gas inside the nuclear ring, and therefore to explain the ring's sharp edge. This is necessary, since the gas distribution has a natural tendency to smooth out any sharp structure, through its small viscosity and velocity dispersion.

Although our best fitting model to observed geometry excludes the possibility that there has been a strong bar in the recent past (700 Myr or so), it does not mean that the galaxy has never been strongly barred. On the contrary, the presence of the three rings (nuclear, inner, and outer ring) suggests the existence of a strong bar in the more distant past. Indeed, the timescale of formation of the outer structures is about one order of magnitude larger than that for the nuclear structures. Therefore the most likely scenario is that the outer ring was resonant with a strong bar several Gyrs ago. Since the present study regards the nuclear region only, the galaxy long-term history cannot be constrained.

8.2. Spheroidal component

NGC 7217 is one of the most spheroid-dominated spirals known (see B95). It has not only the usual concentrated bulge, but also an extended, luminous, nearly spherical halo, suggesting a "bulge" even more extended than the disk. Buta et al. (1995) interpreted this either as the outer regions of the bulge, or as a separate stellar halo component. If this component is added to the central bulge to make the spheroid component, the spheroid-to-disk luminosity ratio is 2.3, an exceptionally large ratio. This peculiarity might explain the regularity of the structures observed in NGC 7217's disk.

Since the galaxy is nearly face-on however, it is difficult to disentangle the contribution of the spheroidal and disk components, and the interpretation in terms of a disk or stellar halo is still uncertain. Also, the mass-to-light ratios of the various components are unknown, making it useful for us to explore several spheroidal-to-disk mass ratios. We note, however, that the observed light ratio between bulge and disk components favors a non-dominant disk component, and therefore also supports run A as the best solution.

8.3. Gas accretion

The gas content has a large influence on the dynamics of the galaxy. A large amount of gas makes the disk more unstable to bar formation, and the formation of rings is only possible with gas present, the stellar nuclear ring being subsequently created through star formation in the gas ring. An important gas inflow toward the center driven by a strong bar can destroy the bar, and thus the gas regulates the bar strength. This process means that a bar is often a transient feature in a galaxy's life, and external accretion is required for a galaxy to experience several bar episodes in a Hubble time (Bournaud & Combes 2002). From a statistical study of bar strength in a large sample of nearby galaxies, Block et al (2002) estimate that a typical galaxy must double its own mass in 10 Gyr through gas accretion.

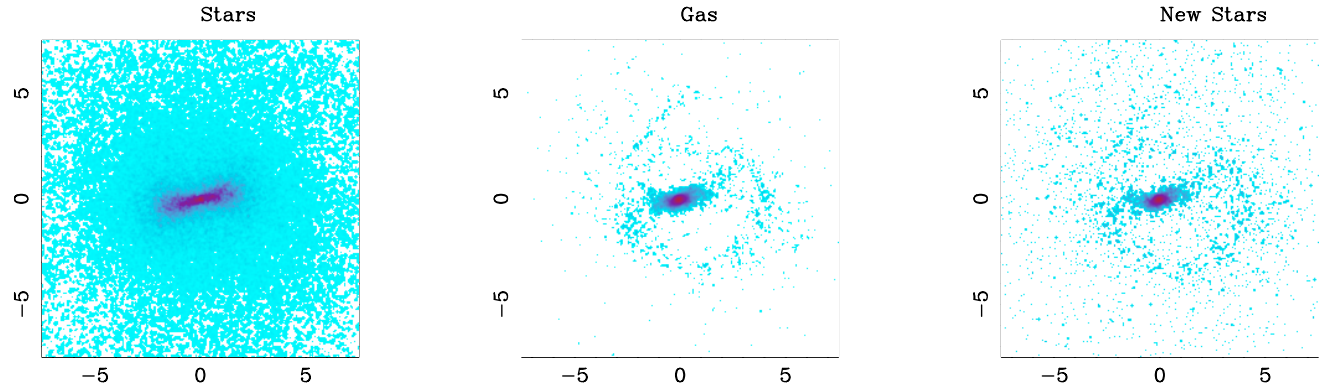

Fig. 23. Left: gray scale plot of the stellar component distribution, in Run B (the gray scale is linear and axes are in kpc). **Middle:** gray scale plot of the corresponding gaseous component (the gray scale is logarithmic). **Right:** plot of the stars formed during the simulation (the gray scale is logarithmic).

A more complete modelling of this galaxy would therefore include gas accretion. However, given the observed low gas fraction of NGC 7217, we do not think it is currently experiencing rapid gas accretion, and so we have not explored models which include a nonzero accretion rate as a free parameter.

9. Conclusion

The molecular gas in the ringed LINER NGC 7217 has been mapped with high resolution (∼150 pc) inside a radius of 1.5 kpc. The CO emission is confined to a broad nuclear ring, remarkably regular and complete. The average radius of the ring is 900 pc, and its width is about 400 pc, covering both the narrow stellar ring (at 750 pc radius) and the multi-armed spiral structure observed in the optical at slightly larger radii. The ring sometimes splits up into several lanes (barely resolved here) that correspond to the spiral structure, fragmented in a few dense clumps. The most striking feature is the sharpness of the inner boundary of the ring. Inside the ring very little emission is found, in particular a nuclear spot of about $5 \times 10^5\ M_\odot$ inside a radius of 70 pc. Almost perfect circular motion is observed in the ring.

The action of an oval distortion is favored to account for the sharp ring edge. The presence of three rings in this galaxy already supports the bar hypothesis, since the locations of the three rings correspond to bar resonances, according to the rotation curve (cf. B95). However, two scenarios are conceivable, either the observed sharp nuclear ring is the consequence of a recent strong bar that has now faded, or a persistent weak oval distortion is sufficient. The two possibilities would have different impacts on fueling of the AGN.

As the rotation curve does not unambiguously separate disk and spheroidal mass components, it is of legitimate interest to explore models with both maximal and minimal disks. These two extreme models were explored with N-body models taking into account the gravity of stars and gas, as well as star formation and feedback. The best fit to the observations is obtained when only a weak bar existed in the recent past, and a large fraction of the original gas mass has been consumed by star formation. The gas was more strongly self-gravitating in the past and formed a very contrasted ring, whose continued high contrast is maintained by the weak oval distortion. This distortion prevents a large quantity of gas from flowing to the nucleus and accounts for the low gas content observed there. In the alternate hypothesis, a strong bar does not lead to the formation of a contrasted ring, but instead drives a lot of gas toward the center. This would have been observed today, unless a nuclear starburst occurred. However the presence of such a nuclear starburst is not obvious from the galaxy colors.

We conclude that the sharp CO ring has been built quite recently, when the galaxy had a weak bar in its disk and a higher gas content. The bar has weakened now into an oval distortion, and the consumption of the gas by star formation has now also weakened its self-gravity, preventing efficient fueling of the AGN.

Acknowledgements. We thank the referee, Jonathan Braine, for a careful reading of the manuscript. We are grateful to F. Gueth for having kindly provided the SHORT-SPACE task, and to Melanie Krips for her help in obtaining the 30 m data. Lourdes Verdes-Montenegro kindly sent the Hα image. In this work, we have used the NED and LEDA databases. S. L. is supported by a Marie Curie Individual Fellowship contract HPMF-CT-20002-01734 from the European Union. The computations in this work have been realized on the Fujitsu NEC-SX5 of the CNRS computing center, at IDRIS.

References

Baker, A. J. 2000, Ph.D. Thesis, Caltech, DAI-B 60/12, p. 6149, (181 pages)
Bertin, G., Lin, C. C., Lowe, S. A., & Thurstans, R. P. 1989, ApJ, 338, 78
Block, D., Bournaud, F., Combes, F., Puerari, I., & Buta, R. 2002, A&A, 394, L35
Böker, T., Calzetti, D., Sparks, W., et al. 1999, ApJS, 124, 95
Bournaud, F., & Combes, F. 2002, A&A, 392, 83
Braine, J., Combes, F., Casoli, F., et al. 1993, A&AS, 97, 887
Buta, R., van Driel, W., Braine, J., et al. 1995, ApJ, 450, 593 (**B95**)
Buta, R., & Combes, F. 1996, Fund. of Cosmic Physics, 17, 95-282
Cardelli, J. A., Clayton, G. C., & Mathis, J. S. 1989, ApJ, 345, 245
Clark, B. G. 1980, A&A, 89, 377
Combes, F. 2001, in GH Advanced Lectures on the Starburst-AGN Connection, INAOE, ed. I. Aretxaga, D. Kunth, & R. Mujica (World Scientific), 223 [astro-ph/0010570]

Combes, F., Debbasch, F., Friedli, D., & Pfenniger, D. 1990, A&A, 233, 82
Combes, F., & Gerin, M. 1985, A&A, 150, 327
de Vaucouleurs, G., de Vaucouleurs, A., Corwin, H. G., et al. 1991, Third Reference Catalogue of Bright Galaxies (New York: Springer Verlag)
Elmegreen, B. G., Elmegreen, D. M., Brinks, E., et al. 1998, ApJ, 503, L119
Elmegreen, D. M., Elmegreen, B. G., & Eberwein, K. S. 2002, ApJ, 564, 234
García-Burillo, S., Sempere, M. J., Combes, F., Hunt, L. K., & Neri, R. 2000, A&A, 363, 869
García-Burillo, S., Combes, F., Eckart, A., et al. 2003a, in Active Galactic Nuclei: From Central Engine to Host Galaxy, ed. S. Collin, F. Combes, & I. Shlosman (San Francisco: ASP), 423
García-Burillo, S., Combes, F., Hunt, L. K., et al. 2003b, A&A, 407, 485 (Paper I)
Guilloteau, S., & Lucas, R. 2000, in Imaging at Radio through Submillimeter Wavelengths, ed. J. G. Mangum, & S. J. Radford (San Francisco: ASP), 299
Hasan, H., Pfenniger, D., & Norman, C. 1993, ApJ, 409, 91
Heckman, T. M., Smith, E., Baum, S., et al. 1986, ApJ, 311, 526
Heckman, T. M., Blitz, L., Wilson, A. S., Armus, L., & Miley, G. K. 1989, ApJ, 342, 735
Ho, L. C., Filippenko, A. V., & Sargent, W. L. W. 1997, ApJS, 112, 315
Holtzman, J. A., Burrows, C. J., Casertano, S., et al. 1995, PASP, 107, 1065
Hunt, L. K., & Malkan, M. A. 1999, ApJ, 516, 660
Knapen, J. H., Shlosman, I., & Peletier, R. F. 2000, ApJ, 529, 93
Kormendy, J., & Bender, R. 1999, ApJ, 522, 772
Leitherer, C., Schaerer, D., Goldader, J. D., et al. 1999, ApJS, 123, 3 (SB99)
Martini, P., Regan, M. W., Mulchaey, J. S., & Pogge, R. W. 2003, ApJ, 589, 774
Meixner, M., Puchalsky, R., Blitz, L., Wright, M., & Heckman, T. 1990, ApJ, 354, 158
Merrifield, M., & Kuijken, K. 1994, ApJ, 432, 575
Mulchaey, J. S., & Regan, M. W. 1997, ApJ, 482, L135
Pogge, R. W. 1989, APJS, 71, 433
Pringle, J. E. 1996, MNRAS, 281, 357
Rix, H.-W., & Zaritsky, D. 1995, ApJ, 447, 82
Schinnerer, E., Eckart, A., & Tacconi, L. J. 2000a, ApJ, 533, 826
Schinnerer, E., Eckart, A., Tacconi, L. J., Genzel, R., & Downes, D. 2000b, ApJ, 533, 850
Schlegel, D. J., Finkbeiner, D. P., & Davis, M. 1998, ApJ, 500, 525
Sellwood, J. A. 1980, A&A, 89, 296
Shlosman, I., Frank, J., & Begelman, M. C. 1989, Nature, 338, 45
Shu, F. H., Tremaine, S., Adams, F. C., & Ruden, S. P. 1990, ApJ, 358, 495
Sil'chenko, O. K., & Afanasiev, V. L. 2000, A&A, 364, 479
Solomon, P. M., & Barrett, J. W. 1991, in Proceedings of the 146th Symposium of the IAU, Dynamics of Galaxies and Their Molecular Cloud Distributions, ed. F. Combes, & F. Casoli (Dordrecht: Kluwer Academic Publishers), 235
Stark, A. A., Bally, J., Gerhard, O. E., & Binney, J. 1991, MNRAS, 248, 14P
Tacconi, L., Schinnerer, E., Gallimore, J. F., et al. 1997, BAAS, 191, 7803
Thornley, M. D. 1996, ApJ, 469, L45
Verdes-Montenegro, L., Bosma, A., & Athanassoula, E. 1995, A&A, 300, 65
Vila-Vilaró, B., Taniguchi, Y., & Nakai, N. 1998, AJ, 116, 1553
Young, J. S., Xie, S., Tacconi, L., et al. 1995, ApJS, 98, 219